



ARTICLE

Research of Microstructure, Phase, and Mechanical Properties of Aluminum-Dross-Based Porous Ceramics

Liang Yu^{1,2,3}, Yuan Liu^{1,2,3}, Xiuling Cao^{4,*}, Yulong Yan^{1,2,3}, Chen Zhang^{1,2,3} and Yanli Jiang^{1,2,3,*}

¹Key Laboratory of New Processing Technology for Nonferrous Metals & Materials, Guilin University of Technology, Guilin, 541004, China

²Guangxi Scientific Experiment Center of Mining, Metallurgy and Environment, Guilin University of Technology, Guilin, 541004, China

³Collaborative Innovation Center for Exploration of Nonferrous Metal Deposits and Efficient Utilization of Resources, Guilin University of Technology, Guilin, 541004, China

⁴Hebei Technology Innovation Center for Intelligent Development and Control of Underground Built Environment, School of Exploration Technology and Engineering, Hebei GEO University, Shijiazhuang, 050031, China

*Corresponding Authors: Xiuling Cao. Email: caoxlhbdz@163.com; Yanli Jiang. Email: 2010043@glut.edu.cn

Received: 27 July 2022 Accepted: 13 September 2022 Published: 07 June 2023

ABSTRACT

In this study, the effect of sintering temperature and the addition of kaolin, a sintering agent, on the microscopic, phase, and mechanical properties of ceramics were investigated using secondary aluminum dross (SAD) as the main component in the manufacturing of ceramics. The basic phases of the ceramics were Al_2O_3 , MgAl_2O_4 , $\text{NaAl}_{11}\text{O}_{17}$, and SiO_2 without the addition of kaolin. The diffraction peaks of MgAl_2O_4 , $\text{NaAl}_{11}\text{O}_{17}$, and SiO_2 kept decreasing while those of Al_2O_3 kept increasing with an increase in temperature. In addition, the increase in temperature promoted the growth of the grains. The grains were uniform in size and regular in distribution, with a shrinkage of 2.2%, porosity of 72.5%, bulk density of 1.076 g/cm^3 , and compressive strength of 1.12 MPa. When the sintering temperature was 1450°C , the basic phases of the ceramic after the addition of kaolin were Al_2O_3 , MgAl_2O_4 , $\text{NaAl}_{11}\text{O}_{17}$, and SiO_2 . With the increase of kaolin, the diffraction peaks of $\text{NaAl}_{11}\text{O}_{17}$ and SiO_2 decreased until they disappeared, while the diffraction peaks of Al_2O_3 increased significantly. When kaolin was added at 30 wt.%, the ceramics obtained had shrinkage of 18%, a porosity of 47.26%, a bulk density of 1.965 g/cm^3 , and compressive strength of 31.9 MPa. Cracks existed inside the ceramics without the addition of kaolin, while the addition of kaolin significantly changed this defect. It is shown that SAD can obtain porous ceramics with good properties at a sintering temperature of 1450°C and a kaolin addition of 30 wt.%.

KEYWORDS

Secondary aluminum dross; porous ceramics; microstrure; phase; mechanical properties

1 Introduction

As a hazardous solid waste generated in the process of smelting aluminum, aluminum dross (AD) can be divided into primary aluminum dross (PAD) and secondary aluminum dross (SAD) based on its aluminum content and the order in which it is generated [1,2]. SAD, also called black ash or black slag ash, is sourced from the ash residue left after the recovery of metallic aluminum from PAD [3], which contains a low



This work is licensed under a Creative Commons Attribution 4.0 International License, which permits unrestricted use, distribution, and reproduction in any medium, provided the original work is properly cited.

amount of metallic aluminum (generally 10% to 20%), and a high contents of other substances such as alumina, silicon oxide, aluminum nitride, inorganic salts, and magnesia-alumina spinel [4,5]. SAD is more difficult to treat, the treatment process is complex, and the high cost of treatment is a series of problems leading to direct landfill disposal in many plants, thereby causing irreparable damage to both soil [6], air [7], and water resources [8]. In recent years, the harmful effects of SAD on the environment have received attention [9]. In addition, the reuse of hazardous solid waste has become a hot topic for scholars to study, particularly solid waste and the materials mixed to prepare ceramics. Gironi et al. [10] used different content of powdered cigarette waste mixed with clay, the shrinkage of ceramic block sintered at a temperature of 900°C was small. As the content of powdered cigarette waste increased, the water absorption of the ceramic block increased, but the compressive strength decreased. When the content of powdered cigarette waste was 5%, a ceramic block with good overall performance was obtained. This study used solid waste mixed with kaolin and sintered at a high temperature to produce ceramic blocks, which can make use of SAD in large quantities.

Before recovering metallic aluminum, alumina and salt from aluminum dross, it is necessary to achieve separation and enrichment of metallic aluminum from other components by means of cooling, crushing, and mechanical separation, which can effectively improve the efficiency of aluminum extraction from aluminum dross [11]. In addition, extracting metallic aluminum can reduce the environmental pollution of the product after arriving at the landfill [12]. The recovered residue still contains a mixture consisting of a high content of Al_2O_3 and MgAl_2O_4 , which can provide a better basis for later sintered ceramics. Foo et al. [13] used two industrial wastes, i.e., fly ash and aluminum dross, as the aluminum and silicon sources for the synthesis of mullite-based ceramics. They made mullite-based ceramics by sintering, and the resulting products showed excellent thermal expansion coefficients with the coefficient of thermal expansion (CTE) values of $4.0\text{--}5.9 \times 10^{-6}\text{°C}^{-1}$. Sooksaen et al. [3] used SAD mixed with aluminosilicate clay and bentonite clay and then sintered it to obtain ceramic refractories. The basic constituent phase of the aluminum dross-based ceramic is $\alpha\text{-Al}_2\text{O}_3$, and the ceramic material obtained was heated at 1200°C and then put to quench in cold water three times without being found to crack, which indicates that the ceramic masses obtained have excellent thermal impact resistance and refractoriness.

In this study, porous ceramics were obtained by high-temperature sintering of SAD as the main raw material doped with easily available kaolin. The objectives of this study were as follows: (1) To obtain the optimum temperature for sintering porous ceramics by using the template method to prepare a ceramic blank with a certain shape. (2) To investigate the optimal content of doped kaolin and the effect on multiple properties of the ceramics. The greatest advantage of this research is the possibility of preparing porous ceramics from large quantities of SAD. Porous ceramics with excellent properties can be obtained with the addition of a small amount of the sintering agent kaolin, and the amount of the sintering agent kaolin added is less expensive and easily available.

2 Experimental

2.1 Characterization of Starting Materials

The SEM and EDS surface sweeps of the SAD after desalination as well as denitrification are shown in Fig. 1, from which it can be seen that O, Al, Na and Si elements are uniformly distributed and Mg elements are aggregated. A point sweep was performed at the Mg element aggregation, and the point sweep is shown in Fig. 2. It can be inferred from the figure that the Mg element aggregation may be mainly composed of MgAl_2O_4 and Al_2O_3 .

In order to further verify the composition of the phase of SAD, X-ray diffractometer (XRD) was used, and the results are shown in Fig. 3. The phase of SAD mainly consists of MgAl_2O_4 and Al_2O_3 , while other phases also contain $\text{NaAl}_{11}\text{O}_{17}$ (Angular islandite), $\text{Al}(\text{OH})_3$, KCl, AlN and $\text{AlO}(\text{OH})$ (Boehmite). It was determined that the Al_2O_3 and MgAl_2O_4 in SAD grow when sintered and given ceramics a certain strength, $\text{NaAl}_{11}\text{O}_{17}$ does not have a significant effect on the ceramic properties, the presence of KCl produces a low melting point glass melt, and AlN and $\text{AlO}(\text{OH})$ decompose at high temperatures to produce Al_2O_3 .

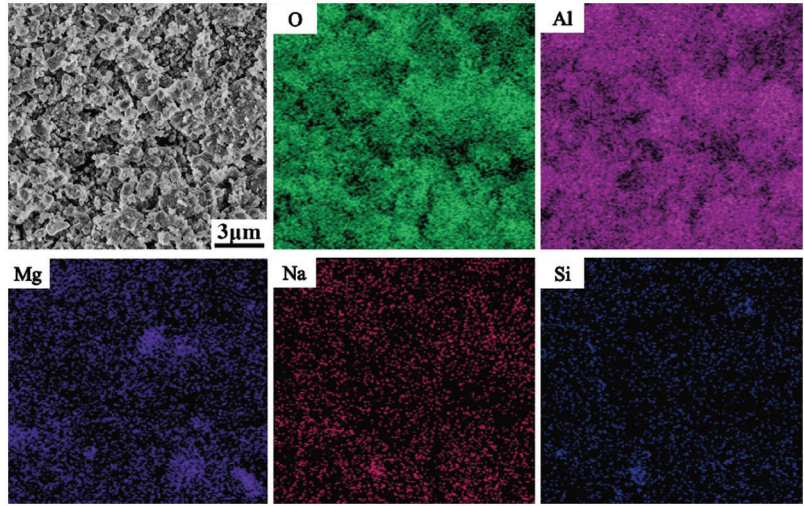


Figure 1: Energy dispersive X-ray spectrometry (EDS) of secondary aluminum dross (SAD)

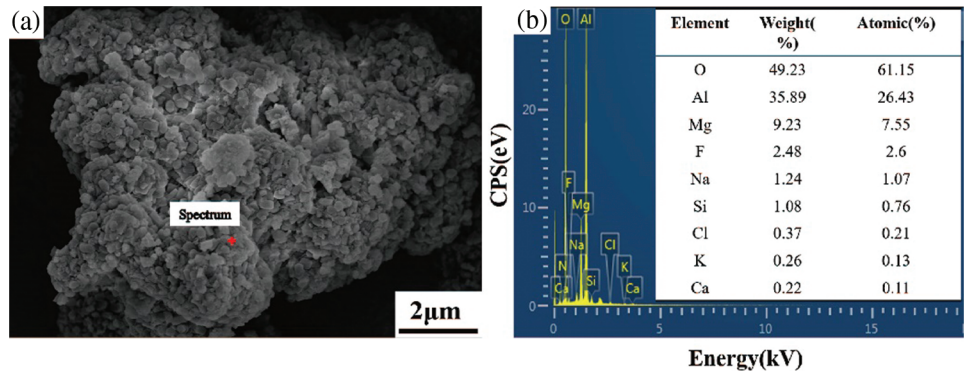


Figure 2: EDS of particles in SAD: (a) SEM image of particles in the SAD, (b) EDS of particle

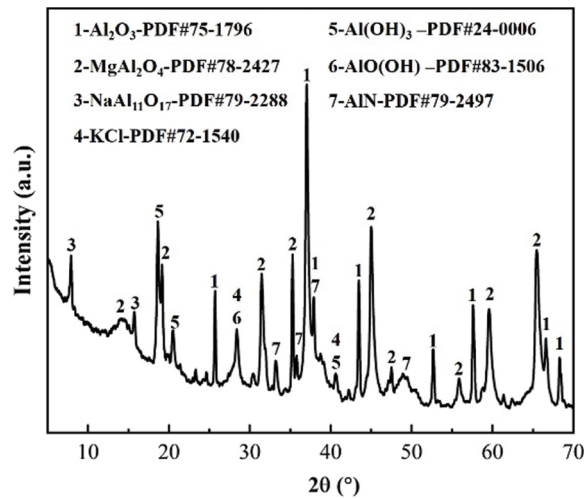


Figure 3: XRD of SAD

The treated SAD was tested by X-ray fluorescence spectrometry, and the main chemical composition was expressed in the form of oxides, as shown in [Table 1](#). It also contained small amounts of elemental F, oxides such as Na₂O, SiO₂, and K₂O, as well as trace compounds that were not detected.

Table 1: Composition of SAD

Composition	Content/%
Al ₂ O ₃	79.757
MgO	9.857
Na ₂ O	2.564
SiO ₂	1.856
CaO	0.8
K ₂ O	0.602
F	2.457
Others	2.107

Among them, MgAl₂O₄ and Al₂O₃ are compounds generated by the oxidation of aluminum and magnesium in metals, while some F elements, Na elements, K elements and chlorides are generated by adding some molten salts during the smelting of aluminum to lower the melting point as well as to prevent oxidation. It was found that NaAl₁₁O₁₇ is an additional product of the smelting process of aluminum, AlN is a nitride formed by molten metallic aluminum under the atmosphere of nitrogen, and Al(OH)₃ and AlO(OH) are products generated during the hydrolysis of AlN [14].

The main chemical composition of kaolin is expressed in the form of oxides, as shown in [Table 2](#).

Table 2: Composition of kaolin

Composition	Content/%
SiO ₂	56.14
Al ₂ O ₃	39.45
CaO	0.57
TiO ₂	0.33
MgO	0.26
Others	3.25

2.2 Methods

Ceramic preparation is divided into the preparation of the green ceramic body and the preparation of the ceramic body, and the main processes are shown in [Fig. 4](#).

Three-dimensional modeling software was used to model, and the experimental molds used MakerBot printer with the PLA rolls as the raw material. Corundum ball mill balls: SAD: anhydrous ethanol were configured in a ratio of 5:1:1 by mass and placed in a 500 ml corundum ball mill jar for ball milling at 350 r/min and 50 min clockwise rotation and 50 min counterclockwise rotation, respectively. After ball milling, the corundum balls were filtered and separated from the aluminum dross slurry, which was dried in a resistance drying oven. After drying, the caked aluminum dross was ground into fine particles using

a mortar and subsequently sieved under a 200-mesh screen. The treated SAD was mixed thoroughly with solvent and additives in a mixer in proportion to the amount of kaolin added as an influencing factor to the ceramics. The ratios of the other components at a kaolin addition of 20 wt.% are shown in Table 3.

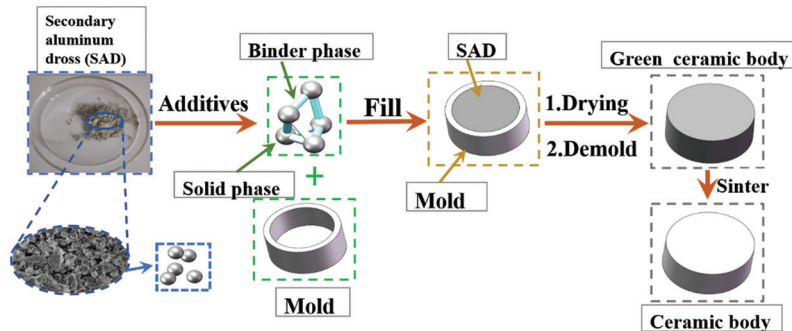


Figure 4: Preparation process of ceramic skeleton

Table 3: Proportion of each component at 20 wt.% kaolin content

Materials	Mass percentage/wt. %
Secondary aluminum dross (SAD)	73.8
Kaolin	20
Polyvinyl alcohol (PVA)	1
Sodium dodecyl sulfate (SDS)	2
Solid defoamer	0.2
Glycerin	3
Deionized water	Depends on kaolin content

The aluminum dross slurry was filled into the mold by hand. To prevent the occurrence of problems such as the slurry not being filled tightly and in place inside the mold, microwave vibration was used required while filling. After filling, drying and dehydration took place. If the moisture content in the green ceramic body was too high, cracks and other defects would be produced during the sintering process of the ceramic. The specific operation was to freeze the billet quickly at -40°C for 4 h until the billet containing water was completely frozen, and after freezing, it was dried in a vacuum freeze dryer at -30°C for more than 5 h. After drying, the molded green ceramic body was removed from the mold.

The dried green ceramic body was put into the muffle furnace, and three temperature gradients were set: The first stage, $30^{\circ}\text{C}\sim 800^{\circ}\text{C}$, with a heating time of 100 min; the second stage, $800^{\circ}\text{C}\sim 1150/1250/1350/1450^{\circ}\text{C}$, with a heating time of 100 min [3]; the third stage, with a holding time of 4 h. After sintering, the ceramic body was cooled to room temperature by using the furnace, and the ceramic body was obtained.

2.3 Sample Analysis

In this study, field emission scanning electron microscopy (SEM, S-4800, Japan) and energy dispersive X-ray spectrometry (EDS, Oberkochen, Germany) were used for microscopic morphology and elemental distribution analysis. SAD and ceramic powder phase compositions were tested using X-ray diffraction (XRD, Xpert Pro, Netherlands) with Cu $K\alpha$ as the radiation source. The analysis of the elemental chemical state of ceramic powders was tested using X-ray photoelectron spectroscopy (XPS, ESCALAB

250Xi, USA). The quantitative analysis of SAD oxides was tested using an X-ray fluorescence spectrometer (XRF, Zetium, Netherlands), while the bonding of ceramic powders used fourier transform in infrared absorption spectrometry (FTIR, Nicolette 6700-NXR, USA) testing. The ceramic strength test used an electronic universal testing machine (AG-20I, China), with test parameters based on the porous ceramic compression strength test method. Three-dimensional visualization of the internal state of ceramics prepared with different kaolin additions to the skeleton used X-ray computed tomography (X-CT, Xradia 510 Versa, Germany).

3 Results and Discussion

3.1 Sintering and Phase Evolution Characterization

3.1.1 Phase and Microstructure at Different Sintering Temperatures

It can be seen from Fig. 5 that the composition of the phase does not change as the temperature increases and is mainly composed of Al_2O_3 , MgAl_2O_4 , $\text{NaAl}_{11}\text{O}_{17}$, and SiO_2 . However, with the increase in temperature, the diffraction peaks of MgAl_2O_4 , $\text{NaAl}_{11}\text{O}_{17}$ and SiO_2 kept decreasing, and the diffraction peaks of Al_2O_3 kept increasing. In particular, the diffraction peak of MgAl_2O_4 decreased the most, mainly because MgAl_2O_4 as AB_2O_4 small cubes, in which there were four oxygen ions, and the oxygen ions in the two coplanar small cubes formed octahedral voids. In contrast, in a spinel unit cell, there are 96 voids, but only 24 were occupied, where the oxygen ions could easily form heterogeneous homophases with other cations. The accelerated diffusion of Na^+ into MgAl_2O_4 at a high temperature led to a decrease in the phase content on the XRD pattern, and the sintering temperature was the dominant factor in the sintering process.

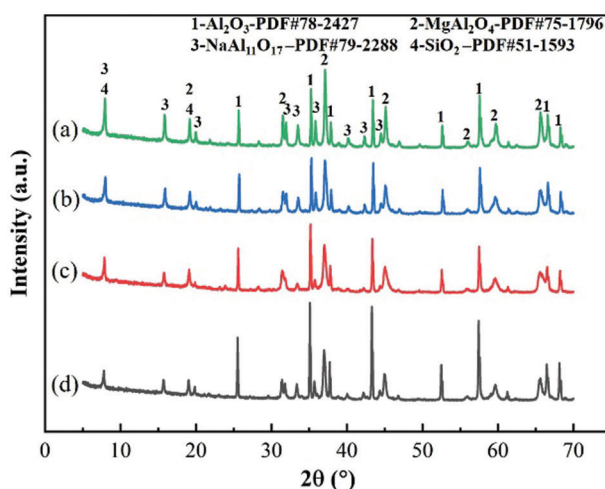


Figure 5: XRD of ceramic powders with different sintering temperatures: (a) 1150°C, (b) 1250°C, (c) 1350°C, (d) 1450°C

The SEM images of the ceramic fractures at different sintering temperatures shown in Fig. 6 exhibited significant solid-phase sintering compared to the raw SAD, where powdered trace compounds on the microscopic surface of the sintered formed was ceramics volatilized or generated new substances at high temperatures. Under high-temperature conditions, the thermal defects of raw material crystals increased as well as heat dispersion and mutual diffusion. The interfaces fused with each other, forming a continuous lamellar phase. However, when the lamellar and granular phase stacking gap was larger, the macroscopic performance of the compressive strength was poor. With the increase in sintering temperature, the

lamellar phases are stacked on top of each other. The presence of element F in the raw material reduced the surface energy of (0001) crystal face [15], while the newly generated (0001) crystal face of the same area required less driving force than the (1010) crystal face, resulting in a faster expansion rate in the (0001) crystal face. As a result, the α - Al_2O_3 particles were anisotropic growth. The alumina particles tended to form a regular lamellar structure. The thickness and size increased, while the overall microstructure was still relatively loose. The presence of F elements could reduce the transformation energy of sub-stable β - Al_2O_3 to stable α - Al_2O_3 [16], which can make the final α - Al_2O_3 appear as a regular hexagonal shape, thus finally obtaining a ceramic with good mechanical properties. Eventually, it was measured that there was a partial loss of element F from sintering at different temperatures, and the loss increased as the temperature increased. The relative content of element F in ceramics sintered at 1150°C is 1.973%, in ceramics sintered at 1250°C is approximately 1.797%, in ceramics sintered at 1350°C is approximately 1.681% and in ceramics sintered at 1450°C is approximately 1.574%. The main reason is that the higher the temperature, the faster the detachment of F^- from the Al^{3+} vacancies in the Al_2O_3 , and the reaction of the detached F^- with water vapor to form HF gas and evaporate.

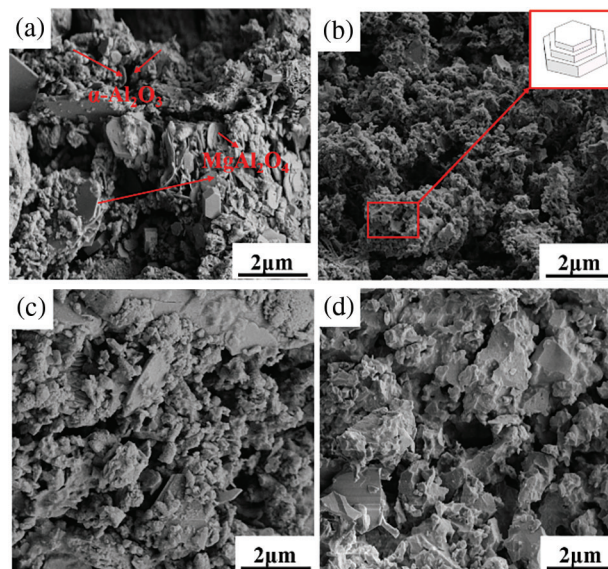


Figure 6: Microscopic morphology of different sintering temperatures: (a) 1150°C, (b) 1250°C, (c) 1350°C, (d) 1450°C

At lower temperatures, pure solid-phase sintering can promote grain growth only by surface diffusion. However, at higher temperatures, grain growth is caused by grain boundary migration, where the rate of grain boundary movement is related to the curvature of the grain boundary as well as the temperature of the system. In other words, the higher the temperature and the smaller the radius of curvature, the faster the rate of grain boundary movement toward its center of curvature. While grain boundary diffusion still exists at this time, the two together promote grain growth [17,18]. Eqs. (1) and (2) were used to describe the relationship between the grain boundary mobility and grain boundary diffusion coefficient [19].

$$B = D_b/RT \quad (1)$$

$$D_b = D_0 \exp(-Q_b/RT) \quad (2)$$

where: B is the grain boundary mobility; D_b is the grain boundary diffusion coefficient; R is the gas constant; T is the sintering temperature; D_0 the constant of grain boundary diffusion.

The higher sintering temperature brings a larger grain boundary mobility and diffusion coefficient, which increases the grain growth rate.

The microscopic morphology of the ceramic section at the sintering temperature of 1450°C (Fig. 6d) shows that the grain size is uniform, the grain arrangement is regular, the proportion of grain boundaries is large, and the crack extension travels longer when damaged along the grain boundaries. As a result, the mechanical strength increased. Therefore, based on the above discussion, the optimal preparation parameter for the aluminum-dross-based ceramics can be determined at a sintering temperature of 1450°C.

3.1.2 Effect of Different Kaolin Additions on Phase and Microstructure

Fig. 7a shows the ceramics without the addition of kaolin, which has an overall sparser microscopic appearance. When the addition amount was 10 wt.%, the lamellar phase occurred to stack and create a three-dimensional interlaced mesh pore channel throughout. When the addition amount was 10 wt.% the solid solution phase was generated during the sintering process, which drove the particle rearrangement and viscous flow. An obvious sintering neck appeared in the microstructure, through which each part carried out the material transfer, thereby causing the migration of pores, shrinkage, and finally, the formation of ceramics with higher strength and better density. When the amount of kaolin added was greater than 20 wt.%, the ceramic section was flatter, and more pores existed on the surface due to the presence of the liquid phase, which filled the gaps and some of the pores. With the increase in kaolin content, the number of pores decreased, but the pore size started to become larger.

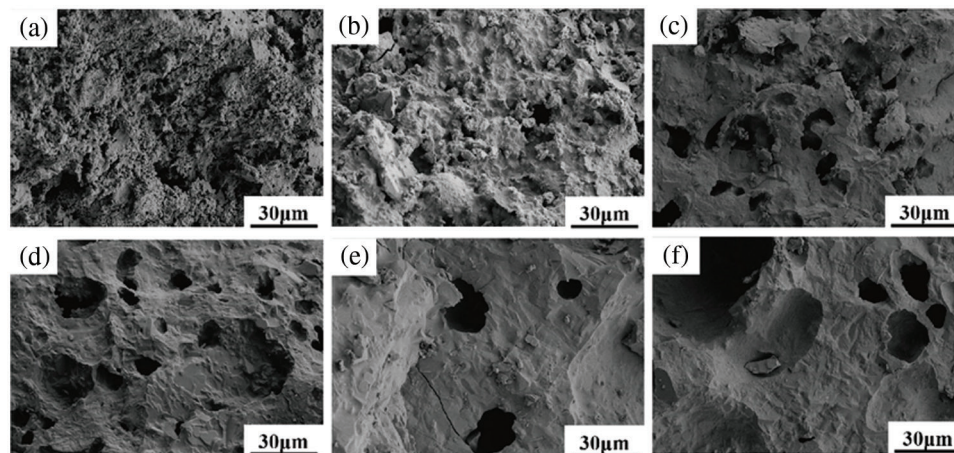


Figure 7: Cross-sectional morphology of sintered ceramics with different kaolin additions: (a) 0 wt.%, (b) 10 wt.%, (c) 20 wt.%, (d) 30 wt.%, (e) 40 wt.%, (f) 50 wt.%

The introduction of the sintering agent kaolin provided an additional source of silicon and aluminum for the ceramic sintering, but the XRD patterns (Fig. 8) showed that the $\text{NaAl}_{11}\text{O}_{17}$ and SiO_2 in the ceramic phase did not increase with the increase of kaolin. Instead, the intensity of the diffraction peaks corresponding to $\text{NaAl}_{11}\text{O}_{17}$ and SiO_2 gradually decreased until they disappeared. The decrease in the diffraction peaks of $\text{NaAl}_{11}\text{O}_{17}$ and SiO_2 as well as their disappearance, did not correspond to the generation of mullite diffraction peaks. This is because the alkali metal oxides reacted with them to produce a low melting point glass melt, which broke the original lattice structure and formed an amorphous material, making it undetectable by XRD. The crystals of mullite were complex, in which there were $[\text{SiO}_4]/[\text{AlO}_4]$ tetrahedral double chains that were not regular, and the double chains were connected by $[\text{AlO}_6]$ octahedra. With the increase of Al^{3+} , the crystal contains more oxygen vacancies, which were not stable and could easily displace the cations. Due to the presence of oxygen vacancies, the

lattice structure of mullite has many voids and is relatively lax. In contrast, the structure of MgAl_2O_4 was more compact, and the $[\text{SiO}_4]$ tetrahedra were only connected by O-Mg-O bonds. The structure was stable, so the diffraction peaks were always present in the XRD pattern. When kaolin was at $T = 400^\circ\text{C} \sim 500^\circ\text{C}$, $\text{Al}_2\text{O}_3 + 2\text{SiO}_2 + 2\text{H}_2\text{O} = \text{Al}_2\text{O}_3 + 2\text{SiO}_2 + 2\text{H}_2\text{O} \uparrow$, the kaolin dehydrated into metakaolin. When kaolin was at $T = 400^\circ\text{C} \sim 1100^\circ\text{C}$, $\text{Al}_2\text{O}_3 + 2\text{SiO}_2 = \text{SiAl}_2\text{O}_4 + \text{SiO}_2$, at about 980°C , the metakaolin transformed to a spinel structure and amorphous SiO_2 . When kaolin is at $T > 1100^\circ\text{C}$, $\text{SiAl}_2\text{O}_4 + \text{SiO}_2 = 1/3(3\text{Al}_2\text{O}_3 \cdot 2\text{SiO}_2) + 3/4\text{SiO}_2$, the spinel reacted with amorphous SiO_2 to form partial primary mullite. The partial, primary mullite reacted with $\alpha\text{-Al}_2\text{O}_3$ to form defective secondary mullite, and the Na atoms entered the secondary mullite with more defects to form an undetectable and amorphous solid solution phase ($\text{Na}_2 \cdot \text{Al}_2\text{O}_3 \cdot 2\text{SiO}_2$) [20].

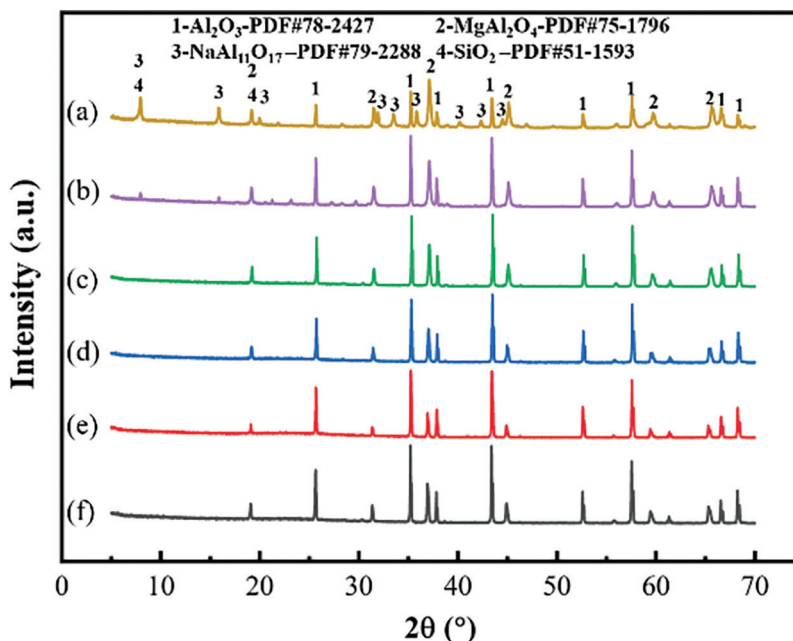


Figure 8: XRD of ceramic powders with different sintering temperatures: (a) 0 wt.%, (b) 10 wt.%, (c) 20 wt.%, (d) 30 wt.%, (e) 40 wt.%, (f) 50 wt.%

In order to verify the speculation of solid solution phase generation, the Si 2p, Na 1s, O 1s and Al 2p electron energy spectra were obtained by detecting and analyzing the ceramics using XPS (Fig. 9). The high-resolution spectra of Si (Figs. 9b–9c) showed that two peaks existed for the skeletal Si 2p of pure SAD sintering and SiO_2 at 98.66 eV with $\text{Na}_2\text{O}-2\text{Al}_2\text{O}_3\text{-SiO}_2$ at 101.99 eV. However, when the 20 wt.% kaolin was added, and the sintered skeletal SiO_2 peak disappeared. This was mainly due to the electron transfer between Na atoms and O atoms belonging to SiO_2 when Na diffused into SiO_2 with structural defects in mullite. With the increase of Al content, the Si was gradually replaced by Al in the Si-O-Si bond to form a Si-O-Al bond, which gradually decreased the SiO_2 phase and generated a solid solution phase [21–23].

Figs. 10a and 10b show the FT-IR absorption spectra of ceramic powders with kaolin addition of 0 wt.% and 30 wt.%, respectively. The peak at 3433.85 cm^{-1} in Fig. 10a is the -OH stretching vibration peak, while the peak at 1629.55 cm^{-1} is the bending vibration peak of H_2O , which is due to the presence of ionized water and free water in kaolin. As a result, drying could not remove the ionized water. 1047.91 cm^{-1} was the stretching vibration peak of the Si-O bond, and 760.64 cm^{-1} was the bending vibration peak of the Si-O-Si bond. The 701.96 cm^{-1} peak corresponded to the bending vibration peak of the Si-O bond, the 590.11 cm^{-1} peak was the bending vibration peak of the Si-O-Al bond in $[\text{SiO}_4]$, $[\text{AlO}_4]$, and the 452.75 cm^{-1} peak corresponded to the bending vibration peak of the Si-O bond.

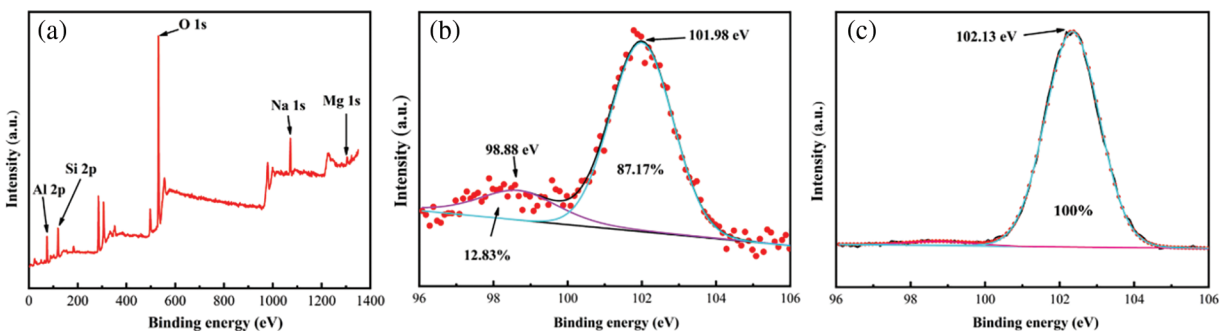


Figure 9: Ceramic of X-ray photoelectron spectroscopy (XPS) curves: (a) full spectrum, (b) 0 wt.% kaolin sintered skeleton Si fine spectrum, (c) 30 wt.% kaolin sintered skeleton Si fine spectrum

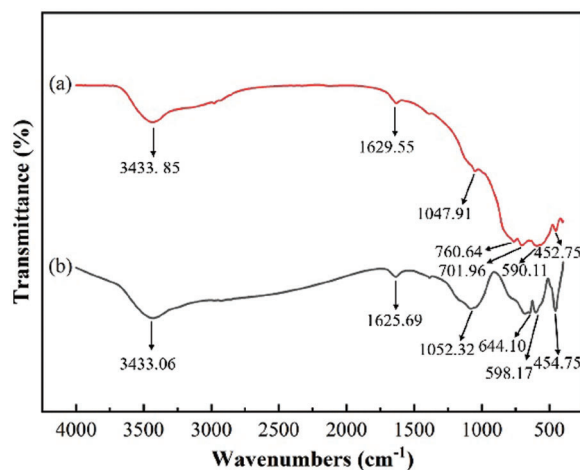


Figure 10: Fourier transform infrared (FT-IR) spectra of sintered ceramic powders with different kaolin additions: (a) 0 wt.%, (b) 30 wt.%

The peak at 644.10 cm^{-1} was the stretching vibration peak of Al-O in $[\text{AlO}_6]$, the peak at 598.17 cm^{-1} was the bending vibration peak of the Si-O-Al bond in $[\text{SiO}_4]$ and $[\text{AlO}_4]$, and the peak at 454.75 cm^{-1} corresponded to the bending vibration peak of the Si-O bond.

The bending vibration peak of the Si-O-Al bond in Fig. 10b became sharper than that of the Si-O-Al bond in Fig. 10a, which further verified that Si was gradually replaced by Al in the Si-O-Si bond to form the Si-O-Al bond.

3.2 Mechanical Properties

3.2.1 Ceramic Shrinkage Rate

The ceramic shrinkage rate is an important basis for determining the stability of ceramic products. If the ceramic shrinkage rate is too small, it will lead to ceramic that is not dense, and more holes will be produced. If the ceramic shrinkage rate is too large, it will affect the later use of performance. A suitable shrinkage rate is a key factor in judging the performance of ceramic products. The shrinkage rate is mainly affected by the amount of kaolin added and the sintering temperature, as shown in Fig. 11.

When the sintering temperature was 1150°C , the shrinkage increased with the increase of kaolin content and reached 8% when the kaolin addition was 50 wt.%. When the sintering temperature was 1250°C and 1350°C , the shrinkage became larger. Shrinkage becomes greater as the kaolin increases, with a

maximum shrinkage of 21%. When the kaolin content exceeded 40 wt.%, the shrinkage started to decrease. When the sintering temperature was 1450°C, the shrinkage increased rapidly with the increase of kaolin content and was maximum at 20 wt.% kaolin, which was 22%. However, the shrinkage started to decrease when the kaolin exceeded 20 wt.%.

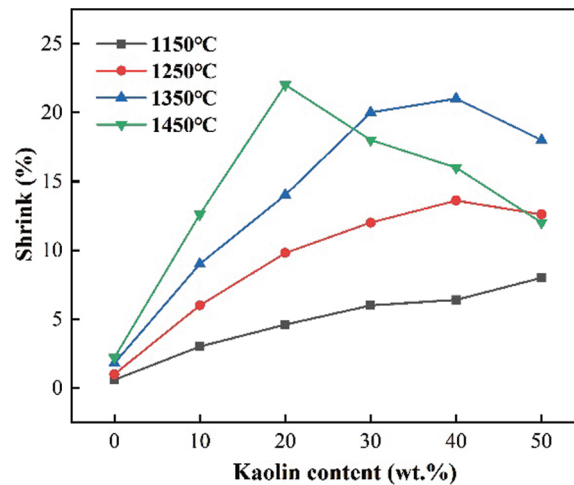


Figure 11: Shrinkage of ceramics at different sintering temperatures and different kaolin additions

3.2.2 Porosity and Bulk Density

In this study, different ceramics were prepared with the sintering temperature as well as kaolin content as variables, and the physical properties of the ceramic skeletons were tested using the Archimedes drainage method, as shown in Fig. 12 for porosity and bulk density. When kaolin was not added, there was a small decrease in porosity from 78.36% to 72.5% and a small increase in bulk density from 0.929 g/cm³ to 1.076 g/cm³ with the increase in temperature. When kaolin was added as the sintering agent, there was a large change in both the porosity and bulk density with an increase in temperature. When the temperature was fixed (1450°C), within 20 wt.% of the addition of kaolin as a sintering agent, the porosity decreased from 72.5% to 29.87%, and the bulk density increased from 1.076 g/cm³ to 2.048 g/cm³. When the addition amount exceeded 20 wt.%, the porosity increased from 29.8% to 58.03%, and the bulk density increased from 2.048 g/cm³ to 1.509 g/cm³.

3.2.3 Compressive Strength

As shown in Fig. 13, the compressive strength of the ceramics had a slight increase with the increase in temperature from 0.054 to 1.12 MPa when kaolin was not added, but when kaolin was added as the sintering agent, the compressive strength increased more with the increase in temperature. The compressive strength of the ceramics showed the best performance at a sintering temperature of 1450°C. The compressive strength increased with the addition of kaolin as a sintering agent within 30 wt.%, and reached 31.9 MPa at 30 wt.%. After the addition of more than 30 wt.%, the compressive strength began to decrease, and with the addition of 50 wt.%, the compressive strength decreased to 25.56 MPa.

There are two broad reasons why the mechanical properties of ceramics changed with temperature and the amount of kaolin added:

Firstly, MgO in kaolin, i.e., the sintering agent, reacted with Al₂O₃ in the matrix at a high temperature to produce MgAl₂O₄ distributed between the Al₂O₃ particles, which inhibited the excessive growth of Al₂O₃ particles and also promoted ceramic densification [24]. However, when too much MgO was added, a

large amount of magnesium aluminum spinel (MgAl_2O_4) was generated, and the accelerated diffusion of Na^+ into MgAl_2O_4 at a high temperature led to a lower phase content on the XRD pattern, which slowed down the growth of Al_2O_3 . Instead, the Al_2O_3 in the ceramics tended to densify, which also explained the increased pores shown in Fig. 7 when the kaolinite addition was greater than 30%.

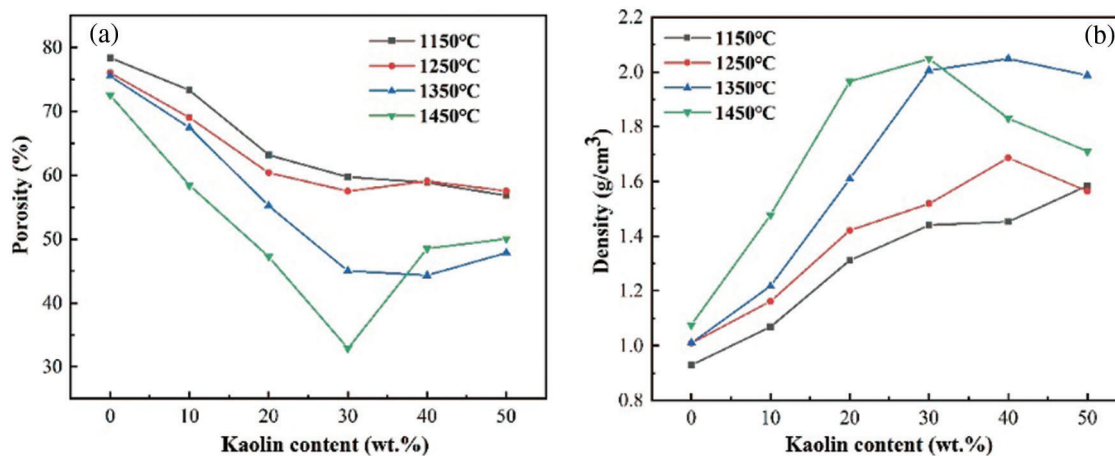


Figure 12: Physical properties of ceramics at different sintering temperatures and kaolin additions: (a) porosity, (b) bulk density

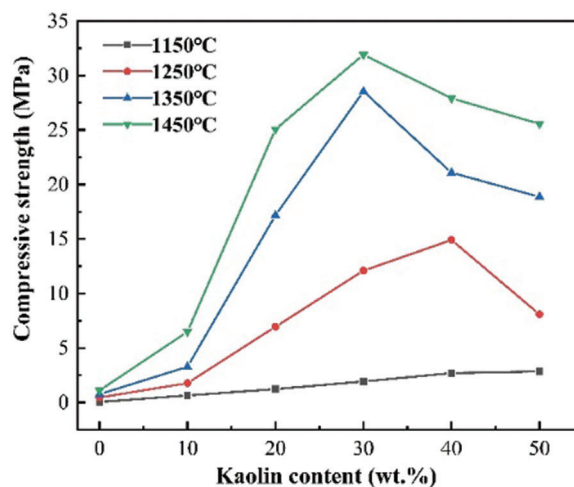


Figure 13: Compressive strength of ceramics at different sintering temperatures and kaolin additions

Secondly, as kaolin was added, its shrinkage increased, and corresponding compressive strength increased. There were also two reasons why this happened: First, kaolin contains more SiO_2 , and with the increase of kaolin addition, its SiO_2 generated mullite ($3\text{Al}_2\text{O}_3 \cdot 2\text{SiO}_2$) with Al_2O_3 at a high temperature. In addition, the mullite belonged to a silicate system, which made the matrix tend to densify. Second, kaolin contains a large amount of SiO_2 phase, as well as a small amount of CaO and TiO_2 , which is a mixed type of sintering aid, thus forming a multi-low eutectic $\text{Ca-Al}_2\text{O}_3\text{-SiO}_2$ with Al_2O_3 , which produced a liquid phase at a lower temperature during the sintering process, largely promoting particle rearrangement and a mass transfer process.

The porous ceramics obtained in this study had excellent mechanical properties and could be used as ceramic reinforcement for ceramic-reinforced composites because of their large number of cavities, which facilitate the penetration of the matrix into the ceramic reinforcement, resulting in a strong bond between the two. Most of the ceramic reinforcements used in the market are produced using organic foam impregnation, which has the advantage of having a large number of holes, but the mechanical properties are poor and not suitable for harsh working conditions. Gonzenbach et al. [25] used organic foam impregnation to obtain a ceramic reinforcement with a compressive strength of 16 MPa, while the ceramic obtained in this study had a compressive strength of 31.9 MPa.

3.3 Ceramic Fault Morphology Characteristics

Fig. 14 shows the internal state of ceramics with different kaolin additions. Fig. 14a shows the internal state of ceramics without kaolin additions. The X and Y axes show the internal cracking of ceramics, which is mainly due to the sudden disappearance of stress during the demolding process and the existence of partial cracks inside [26]. During the sintering process, solid phase sintering plays a major role, and the distance between the particles on both sides of the cracks is larger, making it difficult to diffuse the material and making the cracks larger. Fig. 14b shows the internal state of the ceramics with 10 wt.% kaolin addition. With no cracks and small uniform holes, the liquid phase sintering rearranges the particles to densify the ceramics. Figs. 14c and 14d show the internal state of the ceramics with 30 wt.% and 50 wt.% of kaolin addition, respectively. There were more large pores, and too much kaolin addition generated a large amount of $MgAl_2O_4$ that prevented Al_2O_3 from tending to densify.

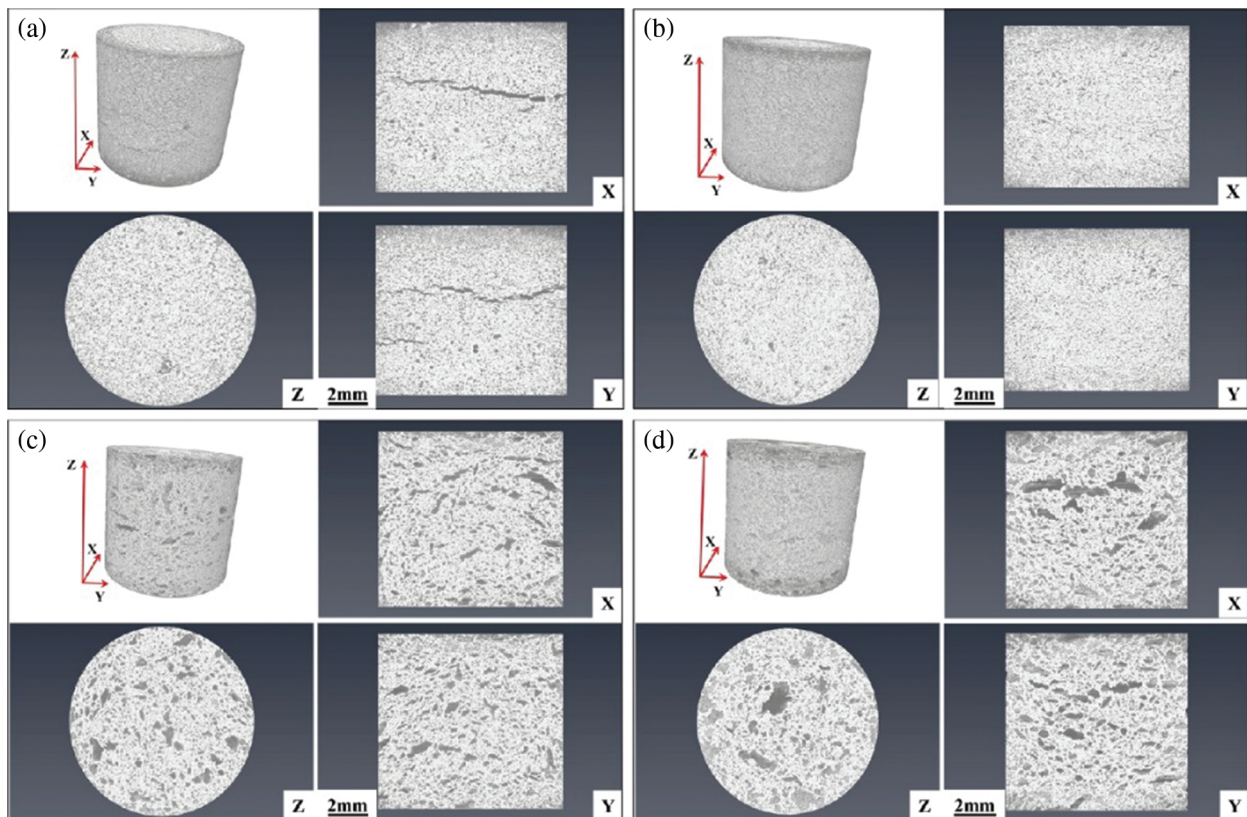


Figure 14: Tomographic scans of ceramics with different kaolin additions: (a) 0 wt.%, (b) 10 wt.%, (c) 30 wt.%, (d) 50 wt.%

4 Conclusion

The effect of different sintering temperatures and different kaolin additions on the ceramics obtained was used to investigate the optimal amount of kaolin additions for the sintering temperature. The XRD and XRF analysis of SAD consisted mainly of Al_2O_3 , MgAl_2O_4 , $\text{NaAl}_{11}\text{O}_{17}$, $\text{Al}(\text{OH})_3$, and KCl phases, which provided raw materials for the sintering of ceramics.

When kaolin was not added, the phase composition of the ceramics obtained did not change as the temperature increased. Instead, the diffraction peaks corresponding to Al_2O_3 increased, the diffraction peaks corresponding to MgAl_2O_4 , $\text{NaAl}_{11}\text{O}_{17}$ and SiO_2 decreased, and the ceramic particles also became compact and uniformly distributed from loose and irregular. The shrinkage, bulk density, and compressive strength of the ceramics increased continuously, and the porosity decreased continuously. At 1450°C , the ceramic shrinkage was 2.2%, the bulk density was 1.076 g/cm^3 , the compressive strength was 1.12 MPa, the porosity was 72.5%, and the compressive strength of the ceramics obtained at this time was poor.

At 1450°C , with the increase of kaolin addition, the diffraction peaks corresponding to $\text{NaAl}_{11}\text{O}_{17}$ and SiO_2 decreased and disappeared at 20 wt.%, and the diffraction peaks corresponding to Al_2O_3 increased. The diffraction peak of MgAl_2O_4 did not change much due to the entry of Na^+ into its lattice. The ceramic section changed from loose to flat. There were more pores and shrinkage, while the bulk density and compressive strength rose first and then fell, with the pores being the first to fall and then rise. When kaolin was added at 20 wt.%, the shrinkage and bulk densities were 22% and 2.048 g/cm^3 at the maximum, the porosity was 29.87% at the minimum, and the compressive strength was 31.9 MPa at 30 wt.%. When kaolin was not added, there were large cracks inside the ceramics, and this defect was obviously solved by adding kaolin.

In general, SAD can obtain porous ceramics with good properties at a sintering temperature of 1450°C and a kaolin addition of 30 wt.%.

Funding Statement: The work was supported by the National Natural Science Foundation of China (51465014), Guangxi Innovation Driven Development Project (Grant No. AA17204021), the Foundation of Guangxi Key Laboratory of Optical and Electronic Materials and Devices (No. 20KF-4), and Foundation of Introduction of Senior Talents in Hebei Province (H192003015).

Conflicts of Interest: The authors declare that they have no conflicts of interest to report regarding the present study.

References

1. Abdulkadir, A., Ajayi, A., Hassan, M. I. (2015). Evaluating the chemical composition and the molar heat capacities of a white aluminum dross. *Energy Procedia*, 75(C), 2099–2105. <https://doi.org/10.1016/j.egypro.2015.07.326>
2. Cao, Y. X., Wang, Z. Q., Wang, J. J., Li, G. F. (2019). Multi-stage electrostatic separation for recovering of aluminum from fine granules of black dross. *Journal of Wuhan University of Technology-Materials Science Edition*, 34(4), 925–931. <https://doi.org/10.1007/s11595-019-2139-2>
3. Sooksaen, P., Puathawee, P. (2016). Conversion of aluminum dross residue into value-added ceramics. *Key Engineering Materials*, 690, 71–75. <https://doi.org/10.4028/www.scientific.net/KEM.690.71>
4. Yang, Q., Li, Q., Zhang, G., Shi, Q., Feng, H. G. (2019). Investigation of leaching kinetics of aluminum extraction from secondary aluminum dross with use of hydrochloric acid. *Hydrometallurgy*, 187, 158–167. <https://doi.org/10.1016/j.hydromet.2019.05.017>
5. Shen, H. L., Liu, B., Christian, E., Zhang, S. G. (2021). Harmless disposal and resource utilization for secondary aluminum dross: A review. *Science of the Total Environment*, 760, 143968. <https://doi.org/10.1016/j.scitotenv.2020.143968>
6. Shinzato, M. C., Hypolito, R. (2016). Effect of disposal of aluminum recycling waste in soil and water bodies. *Environmental Earth Sciences*, 75(7), 628. <https://doi.org/10.1007/s12665-016-5438-3>

7. Li, P., Zhang, M., Teng, L. D., Seetharaman, S. (2013). Recycling of aluminum salt cake: Utilization of evolved ammonia. *Metallurgical and Materials Transactions*, 44(1), 16–19. <https://doi.org/10.1007/s11663-012-9779-3>
8. Li, P., Zhang, M., Wang, Z. B., Seetharaman, S. (2015). BF slag resistance of β - $\text{Si}_3\text{Al}_3\text{O}_3\text{N}_5$ material derived from Al salt cake. *Journal of the European Ceramic Society*, 35(4), 1307–1315. <https://doi.org/10.1016/j.jeurceramsoc.2014.11.002>
9. Mahinroosta, M., Allahverdi, A. (2018). Enhanced alumina recovery from secondary aluminum dross for high purity nanostructured γ -alumina powder production: Kinetic study. *Journal of Environmental Management*, 212, 278–291. <https://doi.org/10.1016/j.jenvman.2018.02.009>
10. Girondi, G. D., Marvila, M. M., Azevedo, A. R. G. D., Charles, C. D. S., Djalma, S. et al. (2020). Recycling potential of powdered cigarette waste in the development of ceramic materials. *Journal of Material Cycles and Waste Management*, 2022, 1672–1681. <https://doi.org/10.1007/s10163-020-01058-7>
11. Meshram, A., Jain, A., Gautam, D., Singh, K. K. (2019). Synthesis and characterization of tamarugite from aluminium dross: Part I. *Journal of Environmental Management*, 232, 978–984. <https://doi.org/10.1016/j.jenvman.2018.12.019>
12. Hwang, J. Y., Huang, X., Xu, Z. (2006). Recovery of metals from aluminum dross and saltcake. *Journal of Minerals and Materials Characterization and Engineering*, 5(1), 47–62. <https://doi.org/10.4236/jmmce.2006.51003>
13. Foo, C. T., Salleh, A. M. S., Ying, K. K., Matori, K. A. (2019). Mineralogy and thermal expansion study of mullite-based ceramics synthesized from coal fly ash and aluminum dross industrial wastes. *Ceramics International*, 45(6), 7488–7494. <https://doi.org/10.1016/j.ceramint.2019.01.041>
14. Kocjan, A., Dakskobler, A., Budic, B., Kosmac, T. (2013). Suppressed reactivity of AlN powder in water at 5°C. *Journal of the American Ceramic Society*, 96(4), 1032–1034. <https://doi.org/10.1111/jace.12237>
15. Li, J., Wu, Y. S., Pan, Y. B., Liu, W. B., Guo, J. K. (2007). Influence of fluorides on phase transition of α - Al_2O_3 formation. *Ceramics International*, 33(6), 919–923. <https://doi.org/10.1016/j.ceramint.2006.02.002>
16. Fu, G. F., Wang, J., Kang, J. (2008). Influence of AlF_3 and hydrothermal conditions on morphologies of α - Al_2O_3 . *Transactions of Nonferrous Metals Society of China*, 18(3), 743–748. [https://doi.org/10.1016/s1003-6326\(08\)60128-4](https://doi.org/10.1016/s1003-6326(08)60128-4)
17. Liu, X. Y., Zou, B., Xing, H. Y., Huang, C. Z. (2020). The preparation of ZrO_2 - Al_2O_3 composite ceramic by SLA-3D printing and sintering processing. *Ceramics International*, 46(1), 937–944. <https://doi.org/10.1016/j.ceramint.2019.09.054>
18. Pan, Y., Li, H., Liu, Y. S., Liu, Y. S., Hu, K. H. et al. (2020). Effect of holding time during sintering on microstructure and properties of 3D printed alumina ceramics. *Frontiers in Materials*, 7, 00054. <https://doi.org/10.3389/fmats.2020.00054>
19. Wagner, A., Holzer, D., Mayrhofer, P. H., Bartosik, M. (2021). Enhanced fracture toughness in ceramic superlattice thin films: On the role of coherency stresses and misfit dislocations. *Materials & Design*, 202, 190517. <https://doi.org/10.1016/j.matdes.2021.109517>
20. Qing, Z. J., Zhou, W. Z., Xia, W. J., Li, H. (2018). Crystallization kinetics, sintering, microstructure, and properties of low temperature co-fired magnesium aluminum silicate glass-ceramic. *Journal of Non-Crystalline Solids*, 486, 14–18. <https://doi.org/10.1016/j.jnoncrysol.2018.02.006>
21. Wang, X. Y., Plackowski, C. A., Nguyen, A. V. (2016). X-ray photoelectron spectroscopic investigation into the surface effects of sulphuric acid treated natural zeolite. *Powder Technology*, 295, 27–34. <https://doi.org/10.1016/j.powtec.2016.03.025>
22. Ivanov, K. S. (2016). Study of sodium silicate system firing during glass ceramic foam preparation. *Refractories and Industrial Ceramics*, 56(6), 621–625. <https://doi.org/10.1007/s11148-016-9900-2>
23. Pongphot, S., Thiansem, S. (2016). The effect of alumina (Al_2O_3) on the characteristics of sintered mullite-cordierite ceramics synthesized with kaolin from Naratiwas of Thailand. *Key Engineering Materials*, 690, 65–70. <https://doi.org/10.4028/www.scientific.net/KEM.690.65>
24. Wang, J., Lim, S. Y., Ng, S. C., Chew, C. H., Gan, L. M. (1998). Dramatic effect of a small amount of MgO addition on the sintering of Al_2O_3 -5 vol% SiC nanocomposite. *Materials Letters*, 33(5), 273–277. [https://doi.org/10.1016/s0167-577x\(97\)00121-3](https://doi.org/10.1016/s0167-577x(97)00121-3)

25. Gonzenbach, U. T., Studart, A. R., Tervoort, E., Gauckler, L. J. (2007). Macroporous ceramics from particle-stabilized wet foams. *Journal of the American Ceramic Society*, 90(1), 16–22. <https://doi.org/10.1111/j.1551-2916.2006.01328.x>
26. Bobylev, S. V., Sheinerman, A. G. (2018). Effect of crack bridging on the toughening of ceramic/graphene composites. *Reviews on Advance Materials Science*, 57(1), 54–62. <https://doi.org/10.1515/rams-2018-0047>